Planetary and Space Science 59 (2011) 661–671

Contents lists available at ScienceDirect

Planetary and Space Science

journal homepage: www.elsevier.com/locate/pss

# First lunar wake passage of ARTEMIS: Discrimination of wake effects and solar wind fluctuations by 3D hybrid simulations

S. Wiehle [a,*], F. Plaschke [b], U. Motschmann [a,g], K.-H. Glassmeier [b,d], H.U. Auster [b], V. Angelopoulos [c], J. Mueller [a], H. Kriegel [a], E. Georgescu [d], J. Halekas [e], D.G. Sibeck [f], J.P. McFadden [e]

[a] Institut für Theoretische Physik der Technischen Universität Braunschweig, Mendelssohnstrasse 3, 38106 Braunschweig, Germany
[b] Institut für Geophysik und extraterrestrische Physik der Technischen Universität Braunschweig, Mendelssohnstrasse 3, 38106 Braunschweig, Germany
[c] Institute of Geophysics and Planetary Physics, University of California, Los Angeles, CA, USA
[d] Max-Planck-Institut für Sonnensystemforschung, Katlenburg-Lindau, Germany
[e] Space Sciences Laboratory, University of California, Berkeley, CA, USA
[f] NASA Goddard Space Flight Center, Greenbelt, MD, USA
[g] Institut für Planetenforschung, DLR, Berlin, Germany

ARTICLE INFO

*Article history:*
Received 7 December 2010
Received in revised form
17 January 2011
Accepted 20 January 2011
Available online 31 January 2011

*Keywords:*
Moon
Lunar wake
ARTEMIS
Hybrid simulation

ABSTRACT

The spacecraft P1 of the new ARTEMIS (Acceleration, Reconnection, Turbulence, and Electrodynamics of the Moon's Interaction with the Sun) mission passed the lunar wake for the first time on February 13, 2010. We present magnetic field and plasma data of this event and results of 3D hybrid simulations. As the solar wind magnetic field was highly dynamic during the passage, a simulation with stationary solar wind input cannot distinguish whether distortions were caused by these solar wind variations or by the lunar wake; therefore, a dynamic real-time simulation of the flyby has been performed. The input values of this simulation are taken from NASA OMNI data and adapted to the P1 data, resulting in a good agreement between simulation and measurements. Combined with the stationary simulation showing non-transient lunar wake structures, a separation of solar wind and wake effects is achieved. An anisotropy in the magnitude of the plasma bulk flow velocity caused by a non-vanishing magnetic field component parallel to the solar wind flow and perturbations created by counterstreaming ions in the lunar wake are observed in data and simulations. The simulations help to interpret the data granting us the opportunity to examine the entire lunar plasma environment and, thus, extending the possibilities of measurements alone: A comparison of a simulation cross section to theoretical predictions of MHD wave propagation shows that all three basic MHD modes are present in the lunar wake and that their expansion governs the lunar wake refilling process.



## 1. Introduction

Since the early time of space flight, the interaction of the Moon with its plasma environment has been investigated with in situ measurements. The first indications of an interaction region of the Moon with the solar wind were found by the IMP-1 satellite (Ness et al., 1964; Ness, 1965). Later, the magnetic field measurements of Lunar Explorer 35, which was injected into a stationary selenocentric orbit, proved the existence of a lunar wake (Ness et al., 1967).

This pioneering mission revealed the low electric conductivity of the Moon, that allows for a fast diffusion of the interplanetary magnetic field through the lunar interior. The basic properties of the lunar interaction with the solar wind is thereby not determined by a magnetosphere, like at Earth. A bow shock is not present. Instead, the incoming solar wind is absorbed by the lunar surface. The Moon does not have an atmosphere which could account for any additional interaction. The dynamics of the interaction are completely characterized by the variability of the solar wind conditions on different time scales. The crustal magnetic field was first investigated by the Apollo missions at the landing sites and from magnetometers aboard the corresponding orbiters. Dyal et al. (1974) give a review on these measurements. An overview of more recent Lunar Prospector measurements is given by Richmond and Hood (2008). These fields, however, do not contribute to the solar wind interaction except at regions very close to the lunar surface. Also, negative charging of the lunar surface was revealed by Lunar Prospector data (Halekas et al., 2002, 2005).

The refilling of the wake created at the night side of the Moon (Lyon et al., 1967) is extended over a large distance downstream because of the supersonic nature of the solar wind. The missing particles in the wake lead to the creation of diamagnetic current

* Corresponding author. Tel.: +49 5313915189.
*E-mail address:* s.wiehle@tu-bs.de (S. Wiehle).

0032-0633/$ - see front matter © 2011 Elsevier Ltd. All rights reserved.
doi:10.1016/j.pss.2011.01.012

systems due to the strong pressure gradients. This causes an increase of the magnetic field magnitude inside the wake and a reduced magnetic field magnitude in its environment (Colburn et al., 1967). Due to their higher thermal velocity electrons cause a charge-separation electric field which slows them down and accelerates the heavier ions into the wake. This effect comes along with a rarefaction wave propagating back into the ambient solar wind, leading to an exponential decrease of the density towards the center of the wake (e.g. Samir et al., 1983). A lunar flyby of the WIND spacecraft proved that these processes occur at the lunar wake (Ogilvie et al., 1996), as predicted by Whang and Ness (1970).

Several full particle and hybrid simulations have treated the lunar wake problem. Charge separation effects were modeled by Birch and Chapman (2002) using a full-particle code while the two ion streams present in WIND observations were also reproduced by Farrell et al. (1998) applying a 1D kinetic approach and by Trávníček et al. (2005) in a 2D hybrid simulation. Kallio (2005) showed the dependence of these ion streams on the magnetic field direction using a 3D hybrid simulation.

Recent results from the spacecrafts Kaguya (Kato et al., 2010), Chang'E (Huixian et al., 2005) and Chandrayaan (Nath Goswami and Annadurai, 2008) show that decades after the first lunar missions new phenomena are discovered, e.g. scattering and pick-up from the surface or magnetic shielding of surface regions (Hartle and Killen, 2006; Saito et al., 2010).

Now we are granted the opportunity to further understand the interaction of the Moon with its plasma environment either within the solar wind (SW) or the distant magnetospheric tail of the Earth. The five spacecrafts NASA mission THEMIS (Time History of Events and Macroscale Interactions during Substorms) has enormously contributed in the last three years to shed new light on different plasma-physical processes, particularly those occurring before and during substorms (Sibeck and Angelopoulos, 2008). For its extended mission called ARTEMIS (Acceleration, Reconnection, Turbulence, and Electrodynamics of the Moon's Interaction with the Sun) the outermost two spacecrafts of the THEMIS constellation (THEMIS-B and THEMIS-C) have been sent to the Moon; they will ultimately be injected into bounded orbits (Angelopoulos, in press; Sibeck et al., in review). During the ARTEMIS main mission phase different orbit types and spacecraft separations will be implemented. The aim is to benefit from simultaneous magnetic field, electric field and particle measurements at two different points in the vicinity of the Moon to allow for a discrimination of temporal and spatial effects.

In early 2010 the two spacecrafts were in a transition phase from their main mission THEMIS orbits around Earth to their new destination. The transition orbits are designed to take advantage of several lunar flybys. During its second lunar flyby, on February 13, 2010, the ARTEMIS P1 spacecraft (previously called THEMIS-B) crossed the lunar wake for the first time. In preparation of the exciting ARTEMIS main mission phase we use magnetic field and plasma measurements from this first wake crossing for an extensive comparison with a hybrid code simulation of the lunar plasma environment around the time of the crossing. Adapted solar wind monitor data from the NASA OMNI database are used as dynamic input for our simulation in order to make it as realistic and comparable to the measured data as possible.

In the first part of this paper, measured and solar wind data, used as simulation input, are described, followed by a brief explanation of the simulation code. Finally, simulation results and their comparison to the data will be presented.

## 2. Measured data and model input

We use Flux-Gate Magnetometer (FGM) magnetic field data in 4 Hz resolution (Auster et al., 2008) as well as particle data from the Electrostatic Analyzer (ESA) instrument (McFadden et al., 2008), in particular the ion density and the plasma bulk velocity for comparison with the simulation results.

Between 08:53 and 09:29 UT on February 13, 2010, the spacecraft was not only located in the lunar wake but was also in lunar shadow, resulting in a thermal cooling of the spacecraft and particularly of its booms. Note that the lunar shadow is not identical to the lunar wake: while the shadow always extends on the Sun–Moon line, the wake expands parallel to the solar wind velocity which may be tilted from this line by several degrees. We refer to the inner wake as the solar wind equivalent to the lunar shadow, i.e. the region void of particles if no refilling took place. Since the THEMIS spacecraft are spin stabilized with a period of roughly 3 s, the contraction of the booms led to a reduction of the moment of inertia and, consequently, to an upward drift in the spin frequency of the spacecraft. While in shadow the correct spin phase cannot be measured via the Sun sensor and, thus, vector quantities cannot be despun correctly. Therefore, the FGM team developed an "eclipse-spin" model to bridge the times of unknown spacecraft spin period, which was derived from magnetic field vector measurements in shadow close to the Earth (dipole dominated) and in the distant tail, where the magnetic field direction is approximately constant. With the help of this model the magnetic field and ion bulk velocity could be despun correctly (Georgescu et al., review).

In this paper, two different coordinate systems are used. The data are given in SSE (Selenocentric Solar Ecliptic) coordinates. The SSE system is essentially the GSE (Geocentric Solar Ecliptic) system with its origin shifted to the Moon. In the simulations, a coordinate system slightly different from SSE is used: While in SSE the $x$-axis points towards the Sun, it points away from the Sun in simulation coordinates. Also the $y$-axis, which points against the direction of Earth' orbit in SSE, is inverted. The $z$-axis, which completes the right-handed system, is the same in both coordinate systems (Fig. 1). For easy comparison to other publications, data plots along the P1 trajectory are all given in SSE while the simulation plots are given in simulation coordinates. The orbit of ARTEMIS P1 during the flyby is displayed in Fig. 2. As can be seen, the spacecraft is always behind the Moon. The orbit does not directly cross the center of the wake, as shown in the right panel.

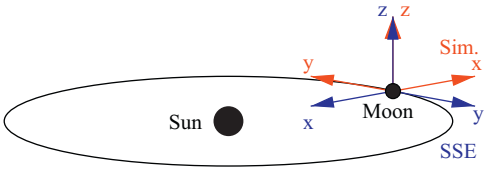


**Fig. 1.** Sketch of the coordinate systems used. In the SSE (Selenocentric Solar Ecliptic) coordinate system (blue), the $x$-axis points towards the Sun, the $y$-axis points against the direction of Earth' orbit, the $z$-axis completes the right-handed system. In the simulation coordinate system (red), the directions of the $x$- and $y$-axes are inverted. (For interpretation of the references to color in this figure legend, the reader is referred to the web version of this article.)

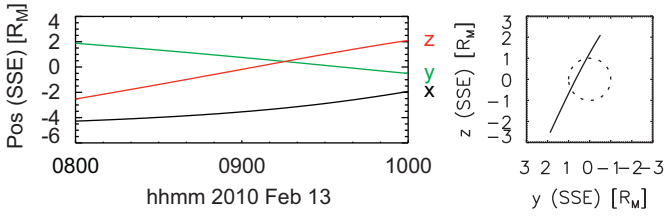


**Fig. 2.** Orbit of ARTEMIS P1 from 08:00 to 10:00 UT. The left plot shows the position in SSE, the right plot shows the $yz$-plane with the dashed circle indicating the radius of the Moon.

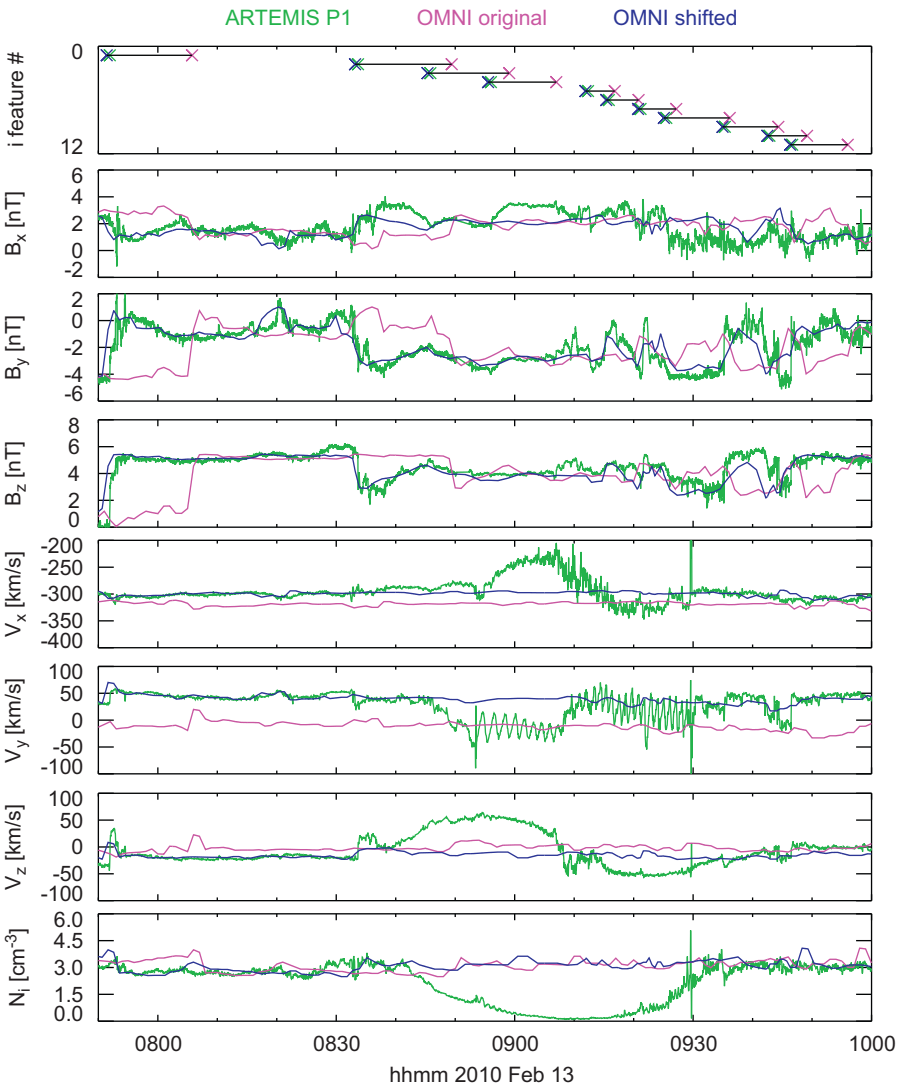


**Fig. 3.** Comparison of time series obtained from ARTEMIS P1 (green) and the OMNI data set (pink, unmodified; blue, time shifted to represent SW data $1.2R_M$ upstream of the Moon). Panels from top to bottom: number of feature $i$ against corresponding time as listed in Table 1, magnetic field ($B_x$, $B_y$ and $B_z$ in SSE: Selenocentric Solar Ecliptic coordinate system), ion bulk velocity ($V_x$, $V_y$ and $V_z$ in SSE), ion density $N_i$. The spacecraft was in lunar shadow between 08:53 and 09:29 UT. During this time a noticeable sinusoidal artifact is visible in the $V_y$ component. (For interpretation of the references to color in this figure legend, the reader is referred to the web version of this article.)

In order to compare the observations performed during the lunar wake crossing with data of the solar wind, we use the high resolution (HRO, 1 min sampling period) magnetic field, ion density and bulk velocity data from the NASA OMNI database. The corresponding data from OMNI and ARTEMIS P1 for the lunar flyby interval are shown in Fig. 3. The OMNI solar wind data are in fact a collection of data from WIND and ACE solar wind monitors. The data of each individual spacecraft have been checked for errors; all samples have been time shifted to represent the solar wind parameters at the bow shock nose of the Earth. A detailed description of the raw measurements and the OMNI database can be found at http://omniweb.gsfc.nasa.gov/html/HROdocum.html. Since the Moon was located upstream of the Earth during the flyby maneuver, the OMNI data (pink lines) show features common to both datasets after they are seen in the ARTEMIS P1 data (green lines, see Fig. 3). This can be seen most clearly for the $B_y$ and $B_z$ components (panels 3 and 4 in the figure).

A constant time shift of the OMNI time series would improve the overall correlation between the two datasets. However, a detailed comparison of the features within the time series reveals that the observed signatures at P1 cannot be explained as the result of propagation with a constant speed over the entire two hour interval of interest. A detailed time shift of each of the visible features would, hence, provide us with much more realistic solar wind conditions to be used as input for our dynamic hybrid code simulation of the lunar plasma environment. Thus, our aim is to time shift different features of the OMNI dataset differently, so that the resulting time series represent the solar wind conditions $1.2R_M$ (Moon radii, $1R_M = 1738$ km) upstream of the Moon (inflow boundary of the simulation box), ready to use for simulation input.

First, the OMNI bulk velocity data are adjusted to match the P1 data in level. For this, vector samples are taken from both velocity datasets between 08:10 and 08:30 UT, where a plateau of constant velocity can be found (see panels 5–7 on Fig. 3). A constant offset is added to the OMNI bulk velocity components, such that the mean values of each component match in the selected interval.

The crosses depicted in the first panel of the figure identify common features in the OMNI magnetic field and ARTEMIS P1 FGM data. Crosses on a common level correspond to the same feature, the color indicates the data set in which the features have been identified (P1, OMNI or shifted OMNI data). The marked times are shown in Table 1. As can be seen the time shift between

**Table 1**
Times of solar wind features identified in both OMNI and ARTEMIS P1 magnetic field time series on February 13, 2010. *i* denotes the number of the feature. The last column indicates the times to which the OMNI features were shifted to represent the SW conditions at $1.2R_M$ upstream of the Moon (simulation box boundary).

| $i$ | OMNI time $t_{i,\mathrm{OMNI}}$ (UT) | P1 time $t_{i,\mathrm{P1}}$ (UT) | Time $1.2R_M$ upstream $t_{i,1.2R_M}$ (UT) |
|---|---|---|---|
| 1 | 08:05:46 | 07:51:56 | 07:51:24 |
| 2 | 08:49:25 | 08:33:40 | 08:33:10 |
| 3 | 08:59:05 | 08:45:50 | 08:45:21 |
| 4 | 09:07:00 | 08:56:00 | 08:55:31 |
| 5 | 09:16:50 | 09:12:20 | 09:11:53 |
| 6 | 09:20:50 | 09:15:50 | 09:15:23 |
| 7 | 09:27:10 | 09:21:10 | 09:20:44 |
| 8 | 09:36:10 | 09:25:30 | 09:25:05 |
| 9 | 09:44:20 | 09:35:20 | 09:34:57 |
| 10 | 09:49:10 | 09:42:50 | 09:42:28 |
| 11 | 09:56:00 | 09:46:40 | 09:46:19 |

the features (pink vs. green color) decreases from roughly 14 min to less than 10 min during the interval of interest. From the P1 reference times (green crosses) we subtracted intervals accounting for the SW convection between the simulation box boundary ($1.2R_M$ upstream) and the $x$-components of the spacecraft position ($r_{\mathrm{P1},x}$) in the SSE coordinate system:

$$t_{i,1.2R_M} = t_{i,\mathrm{P1}} + \frac{1.2R_M - r_{i,\mathrm{P1},x}}{v_{i,\mathrm{OMNI},x}} \quad (1)$$

Here, $t_{i,1.2R_M}$ would be the time of the particular feature $i$ at the simulation box boundary, $t_{i,\mathrm{P1}}$ is the time measured at P1 (third column in Table 1) and $v_{i,\mathrm{OMNI},x}$ is the plasma bulk velocity of the given feature taken from the OMNI dataset at the corresponding times (pink crosses and second column in Table 1). The OMNI dataset time series (magnetic field, velocity and density) are time shifted as well as stretched or compressed by linear interpolation, such that the feature times $t_{i,\mathrm{OMNI}}$ (pink crosses) match the calculated times $t_{i,1.2R_M}$ (blue crosses). A comparison of the time modified OMNI data with the P1 data can be seen in Fig. 3. It shows that the level of agreement between the shifted OMNI and ARTEMIS P1 data is very good for the $B_y$ and $B_z$ components and less good for the $B_x$ component. The velocity components and the density are rather featureless apart from the data within the lunar wake, where both data sets should not and, indeed, do not coincide.

The shifted OMNI time series show features ahead of the P1 data since they represent now SW conditions $1.2R_M$ upstream of the Moon. We used these time series as input for our hybrid code plasma environment simulation.

## 3. The hybrid model

The simulations for this study were performed using the 3D hybrid plasma simulation code A.I.K.E.F. It is an updated version of the code which was originally presented by Bagdonat and Motschmann (2002). Variations of this code have been applied numerous times before (e.g. Simon et al., 2009; Kriegel et al., 2009); hence, only a brief explanation will be given here.

The hybrid model treats ions as macroparticles, solving their equation of motion, whereas electrons are treated as a massless, charge-neutralizing fluid. The motion of ions is governed by the Lorentz force; the electron inertia and displacement current are neglected in this approach because of the slow ion dynamics. An explicit expression for the electric field $\vec{E}$ is obtained from the momentum conservation equation:

$$\vec{E} = -\vec{v}\times\vec{B} + \frac{(\nabla\times\vec{B})\times\vec{B}}{\mu_0\rho_c} - \frac{\nabla P_e}{\rho_c} + \eta\frac{\nabla\times\vec{B}}{\mu_0}. \quad (2)$$

Here, $\vec{v}$ is the ion bulk velocity, $\vec{B}$ the magnetic field, $\rho_c = qn_i$ the charge density, where $n_i$ is a plasma density, and $\eta$ an applied resistivity particularly important for the simulation of the lunar interior. The magnetic field equation is derived from Eq. (2) by applying Faraday's law. The adiabatic law for the electron pressure completes the set of equations, the electron pressure is isotropic ($P_{e,\parallel} = P_{e,\perp}$). The initial temperature distribution of ions and electrons is Maxwellian, but this is not enforced afterwards, any distribution may arise during the simulation.

The interior of the Moon is modeled in analogy to previous studies of conducting obstacles; i.e. Rhea (Roussos et al., 2008), Tethys (Simon et al., 2009) and Enceladus (Kriegel et al., 2009). All particles entering the obstacle are removed, but no boundary conditions are applied for the electromagnetic fields. By including the last term in Eq. (2), electromagnetic field propagation inside the obstacle can be modeled self-consistently. The reciprocal density $1/\rho_c$ and the velocity $\vec{v}$ are set to zero inside the obstacle. As a discontinuity in the density must be avoided for numerical reasons, a density of $10^{-6}$ of the background value is used for the field calculation inside the obstacle. For the simulation, the conductivity of the Moon was set to $1/\eta = 10^{-7}$ S/m. This ensures numerical stability and is also within the range of results given by Dyal et al. (1974). Additionally, a minimum charge density of 0.15 of the background value is used in the field calculations as the $1/\rho_c$ division in Eq. (2) would diverge otherwise. This is especially important within the lunar wake where the plasma density is very low.

The simulation is performed on a Cartesian grid with 112 nodes and a spatial extension of $6R_M$ in each direction. In units of local proton inertia length $x_0$, one lunar radius is about $13.5x_0$ while one simulation cell extends over $0.72x_0$, which makes a hybrid simulation necessary for this situation. The Moon has been placed close ($1.2R_M$) to the solar wind inflow boundary of the simulation box to see a larger part of the lunar wake. The simulation box, hence, extends from $-1.2R_M$ to $4.8R_M$ in $x$-direction and $\pm 3R_M$ in $y$- and $z$-directions.

The rear side of the Moon is a critical region as the simulation code requires the presence of plasma for electromagnetic field convection. Usually, these fields would not be convected inside a vacuum region like the lunar cavity. Therefore, a second ion species consisting of protons with solar wind velocity is inserted

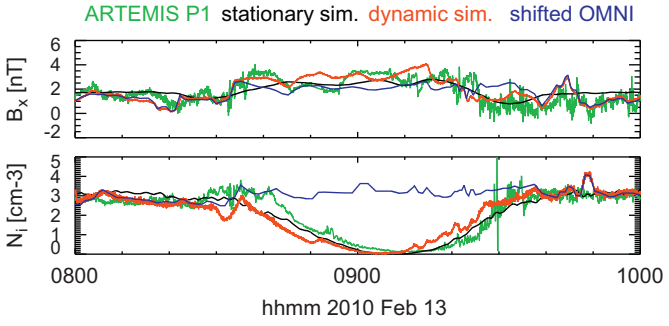


**Fig. 4.** Comparison of the ARTEMIS data (green), the modified background solar wind data (blue), the stationary simulation (black) and the dynamic simulation (red). The upper panel shows the $x$-component of the magnetic field (SSE), the lower panel shows the ion density. The dynamic simulation aligns better to the data due to its ability to follow the strong solar wind fluctuations. (For interpretation of the references to color in this figure legend, the reader is referred to the web version of this article.)

behind the Moon. The density of this species is very low (approx. $10^3$ times below solar wind density) so it does not cause any visible effect to the total density. However, these particles allow the electromagnetic field convection to continue. Lipatov et al. (2005) use the same approach for a lunar-like extra-solar planet and Trávníček et al. (2005) use a very similar approach by having some particles propagate through the Moon. The use of a simplified plane model for the Moon as applied in Farrell et al. (1998), Lipatov et al. (2005) cannot be used here as modeling the propagation of the dynamic inflow through the entire Moon is an essential part of this study.

In the simulations the plasma $\beta$ is set to $\beta_i = 0.2$ for the solar wind ions and $\beta_e = 0.5$ for the electrons. These parameters provide us the best fit of the data. Simulations with plasma betas slightly below 1, suggested by OMNI data, lead to a faster refilling of the wake: Along the ARTEMIS trajectory, the lowest density would then be at about 60% of the background value and the magnetic field magnitude would increase up to a factor of 2; this, however, is not observed in the data.

For the dynamic simulation of the complete flyby, the OMNI solar wind data, modified as described in Section 2, are used as inflow parameters for the simulation. The solar wind magnetic field, velocity and density values at the inflow boundary are adjusted every second. The OMNI data are used for the entire $-x$ simulation boundary. For the magnetic field, this means that $\nabla \cdot \vec{B} = 0$ is initially not fulfilled, as $dB_y/dy = dB_z/dz = 0$, but $dB_x/dx \neq 0$. However, the changes between two successive values are small as the OMNI data, provided in 1 min resolution, are interpolated to 1 s resolution. In comparison to the current density, the resulting divergence is two orders of magnitude

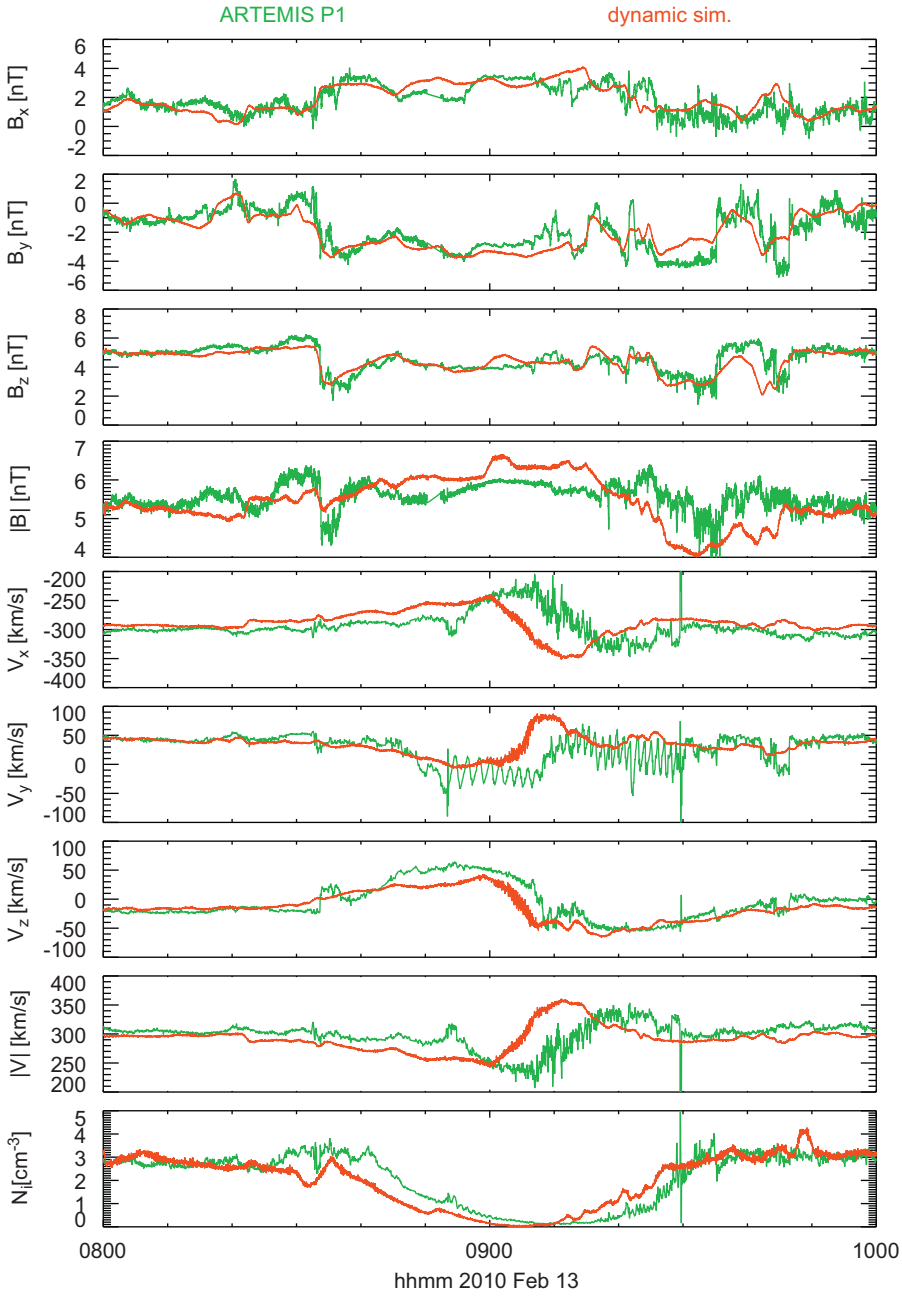


**Fig. 5.** Comparison of the ARTEMIS data (green) and the dynamic simulation (red). Through the dynamic simulation method, a high degree of agreement is achieved despite the strong solar wind fluctuations, where most of the variations in the magnetic field originate (see Figs. 4 and 6). (For interpretation of the references to color in this figure legend, the reader is referred to the web version of this article.)

lower. Thus, the error introduced by the dynamic inflow adjustment is neglectable.

## 4. Results

Two simulations were performed in order to separate the effects of varying solar wind conditions and the lunar wake itself: First, a stationary simulation was performed to study the general effects of the lunar wake. Its input parameters were set to the mean values taken from 8:35–8:37 and 9:32–9:34 UT of the data, shortly before ARTEMIS enters and after it exits the wake; the first interval starts after the main magnetic field rotation occurring at 8:30 UT. The solar wind magnetic field was set to $\vec{B}_{sw} = (1.71, -4.49, 2.80)$ nT (SSE), the solar wind speed was set to $\vec{v}_{sw} = (-295.6, +31.6, -5.2)$ km/s (SSE), and $N_{sw} = 3.14\ \mathrm{cm}^{-3}$ was used as background density. Secondly, a dynamic simulation was performed which covers the entire passage event in real-time. This simulation uses the modified OMNI solar wind data (as described in Section 2) as input parameters.

### 4.1. Dynamic vs. stationary simulation

In Fig. 4, the two simulations, the modified OMNI-data and the ARTEMIS data for the density and the magnetic field $x$-component (SSE) are shown. The presence of the lunar wake is best seen in the solar wind density, shown in the lower panel. Here, a decrease to almost vacuum level occurs between 08:40 and 09:40 UT. Several fluctuations are present in the data and in the dynamic simulation around 09:15 UT. These might be interpreted as an intrinsic instability of the wake. However, a comparison to the OMNI data shows that these fluctuations are already present in the solar wind, and thus they are not a result of the lunar wake interaction. Also, the stationary simulation does not show these effects. Thus, the comparison between P1 data, simulations and solar wind data allows for identification and separation of those effects caused by the solar wind and those caused by the lunar wake.

The upper panel of Fig. 4 displays the $x$-component of the magnetic field. Most of the variations and apparent wave-like patterns originate in the solar wind and the dynamic simulation reflects these variations. The effect of the lunar wake is seen by an increase of the magnetic field inside the wake and a slight decrease at the wake's flanks, which matches the general interaction pattern (Whang and Ness, 1970). Inside the wake, dynamic simulation and OMNI data are comparable, except for a systematic shift of about 1 nT; the magnetic field strength in $x$-direction is increased, but no additional structures are found. This can be seen also in the stationary simulation results: $B_x$ is also increased even though it does not follow the solar wind structures. A comparison based on the stationary simulation alone would hardly clarify the situation because the solar wind induced perturbations are of the same order of magnitude as the lunar wake effects.

In both panels of Fig. 4, it can be seen that the dynamic simulation reflects the data better than the stationary simulation. Thus, in the following, the data are only compared to the dynamic simulation results. The stationary simulation is used to depict the wake structure and for the wave propagation analysis discussed below.

### 4.2. Comparison of data and dynamic simulation

All simulated components of the magnetic field are in good agreement with observations (Fig. 5). The $x$-component was already discussed above. In the $y$- and $z$-components, many patterns are found that appear to show a wave excitation. A comparison to the solar wind background, exemplarily shown for the $y$-component from 09:10 to 09:40 UT in Fig. 6, however,

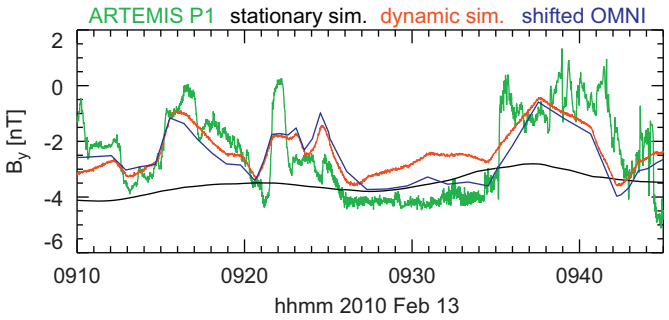


**Fig. 6.** Comparison of the ARTEMIS data (green), the modified background solar wind data (blue), the stationary simulation (black) and the dynamic simulation (red). The $y$-component of the magnetic field (SSE) from 09:10 to 09:45 UT was selected for this plot. (For interpretation of the references to color in this figure legend, the reader is referred to the web version of this article.)

reveals the source of these patterns: All of these are contained in the solar wind; also the stationary simulation does not reflect them. On the contrary, the lunar wake apparently has almost no influence in the $y$- and $z$-components. The observed fluctuations are all due to the solar wind variations, once more showing the importance of their consideration in the simulation.

In contrast to the magnetic field, the solar wind variations in the velocity are much weaker than the influence of the lunar wake as to be seen in the four middle panels of Fig. 5. All components show a counterstreaming as could be expected from previous studies (e.g. Ogilvie et al., 1996). This is clearly seen by the sinusoidal structure with a relatively sharp transition point at about 09:10 UT. The structure is present in all components because the magnetic field is not aligned to one of the coordinate axes; thus, it is difficult to see by eye that the direction of the counterstreaming is indeed parallel to the magnetic field direction. This can be seen more clearly in the plots of the simulation results given in Fig. 9.

The velocity data presented here may still contain some misalignment with the true velocity, caused by the model based spin correction. The correction only had to be applied to the $x$- and $y$-components; the $z$-component was parallel to the spin axis and did not need to be despun. The fast fluctuations during lunar shadow times are caused by the operation of the ESA in magnetospheric mode instead of solar wind mode (McFadden et al., 2008), leading to a reduced angular resolution of ion measurements.

While we can state that the simulation qualitatively agrees with the data in the $x$- and $y$-components, only the $z$-component of the velocity will be discussed in more detail. The simulation does not fully cover the velocity increase in $V_z$ around 08:50 UT before the transition point, where the velocity components transverse to the wake change sign. The reason might be that the refilling of the wake is triggered by charge separation electric fields, which do not occur in this simulation as quasi-neutrality is always assumed. After the transition point two bumps are present in the simulation and several fluctuations in the measured velocity $V_z$. A detailed view on this is given in Fig. 7. Here, we find the solar wind velocity to be relatively stable and also find one bump in the stationary simulation; these bumps must be related to the wake particle refilling process and may indicate the presence of a complicated inner wake vortex structure. This inner wake region is an unstable area, and thus the effects might be caused by a two-stream-instability.

In this figure, the stationary simulation seems to fit the data better than the dynamic simulation. This indicates that the mean values match the conditions during the inner wake passage quite well. The wake direction in the Sun–Moon reference system is strongly dependent on the solar wind velocity; a slightly different

velocity direction causes a tilt of the wake. The results of the simulation along the P1 trajectory, however, depend on the direction of the wake in the simulation box. A small offset might be present in the shifted OMNI velocity data (compared to the real velocity), which probably accounts for the difference between the P1 data and the results of the dynamic simulation.

### 4.3. Simulation results

As an overview to the interaction region, Fig. 8 shows the results of the stationary simulation in the *xz*- and *xy*-planes. Note that the simulation plots use the simulation coordinate system explained in Fig. 1. The Moon is very close to the left (inflow) boundary. These plots show the general features of the lunar wake.

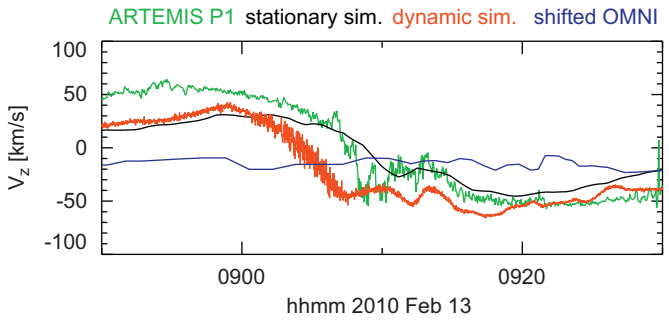


**Fig. 7.** Comparison of the ARTEMIS data (green), the modified background solar wind data (blue), the stationary simulation (black) and the dynamic simulation (red). The *z*-component velocity (SSE) from 08:50 to 09:30 UT is shown here. (For interpretation of the references to color in this figure legend, the reader is referred to the web version of this article.)

In the density panels (a) and (d), the lunar wake is best seen as a region of very low solar wind density behind the Moon. Comparing (a) with (d), we see that the refilling of the wake is not symmetric: At the right boundary of the simulation box, the wake is thinner in panel (a) than in panel (d). Further away from the wake center, a region of decreased density expands: the rarefaction wave, which propagates away from the inner wake. An area with a density on background level is visible between the inner wake and the rarefaction wave at 45 $x_0$ downstream; the wave has apparently separated from the wake. As can be seen, the lunar wake expansion is not parallel to the Sun–Moon line. This is due to the fact that the solar wind is not incident directly from the *x*-direction but has some small velocity components in the *y*- and *z*-directions as well; about 30 km/s of the *y*-component are caused by the motion of the Moon (with the Earth) around the Sun (aberration effect). These components account for the small tilt of the wake.

In the velocity panels (b) and (e) of Fig. 8 both a region with increased and decreased velocity magnitude is found. This velocity distortion is reduced with increasing distance to the Moon. The reason for this effect is the tilt of the interplanetary magnetic field as sketched in Fig. 10, it is better seen in the plots of the *yz*-plane in Fig. 9.

The magnetic field shown in panels (c) and (f) is increased inside the lunar wake by about 30%, but is lower at the edges of the wake by about 10%. This is in accordance to of the data. The simulation plot gives a good overview of this basic interaction

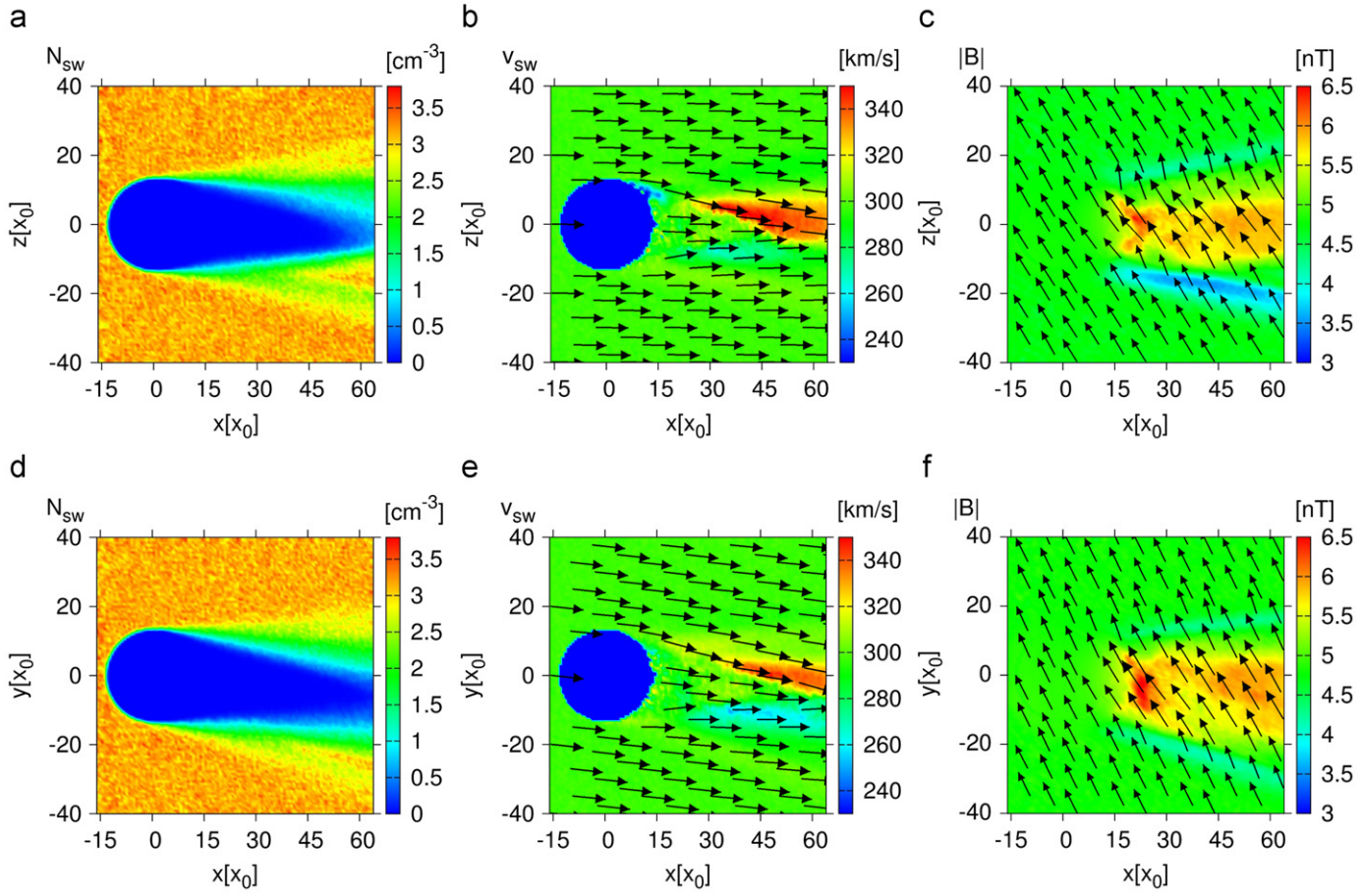


**Fig. 8.** Results of the stationary simulation: *xz*-plane (top row) and *xy*-plane (bottom row). The formation and expansion of the lunar wake are seen in the density plots, panels (a) and (d). The velocity magnitude inside the wake is asymmetric (panels (b) and (e)). The magnetic field magnitude is increased inside the wake (panels (c) and (f)).

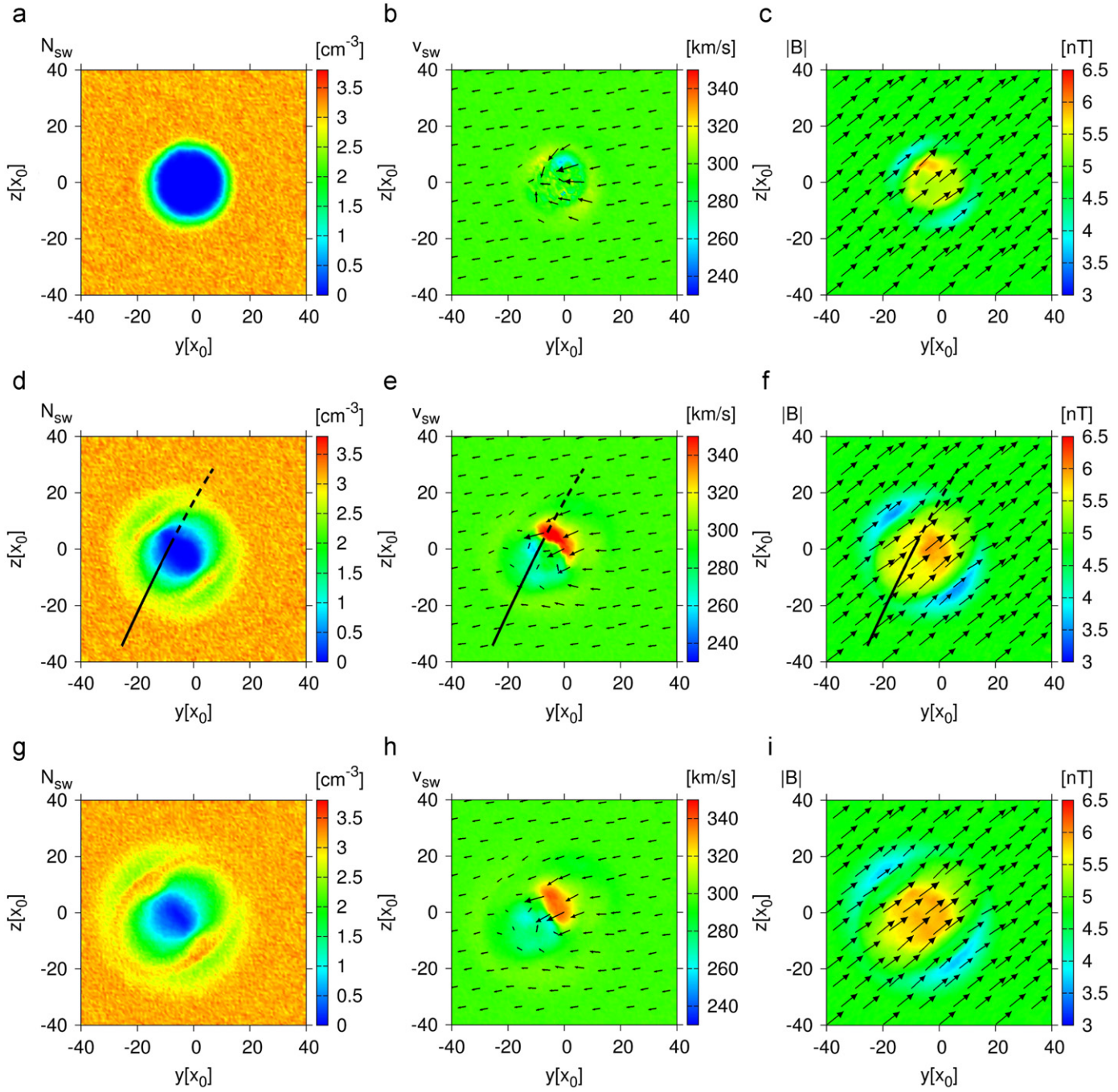


**Fig. 9.** Results of the stationary simulation, *yz*-plane. The cuts were taken behind the Moon at distances of $1.2R_M$, $3.5R_M$ and $4.8R_M$ (top to bottom). The plots show solar wind density, velocity and magnetic field (left to right). The trajectory is shown in the $3.5R_M$ cuts as the transition region is crossed at this distance. The solid black line shows the part of the trajectory in front of each plane, the dashed line the part behind the plane shown.

structure, which is caused by diamagnetic currents when the wake is refilled (Colburn et al., 1967).

For a detailed view of the magnetic field influence, Fig. 9 shows cuts through the *yz*-plane of the simulation box. These cuts are taken at $1.2R_M$, $3.5R_M$ and $4.8R_M$ downstream (top to bottom), respectively. The depicted quantities are (from left to right) the solar wind density, the solar wind velocity and the magnetic field. In the middle row at a distance of $3.5R_M$, the ARTEMIS trajectory, projected to the displayed plane, is shown. Note that it only reaches the border of the inner wake region, as also indicated by the lack of a zero-density plateau in the density plot in Fig. 5.

In the density plots (a), (d) and (g), the asymmetric expansion of the lunar wake can be well observed. The asymmetry is parallel to the magnetic field direction. The rarefaction wave expands orthogonally to the magnetic field and, as visible in panel (g), is detached from the inner wake at this distance ($4.8R_M$).

Panels (b), (e) and (h) of Fig. 9 show the solar wind velocity magnitude. Behind the Moon, the lunar wake is refilled by the surrounding plasma. In panel (b), very close to the Moon, the refilling still appears to be almost symmetric, the asymmetry caused by the magnetic field being very weak. This is different in panels (e) and (h) (higher distance to the Moon) where areas of

increased and decreased velocity have formed. Their boundary is in principal orthogonal to the magnetic field direction, but some distortions are present. Here, the reason for the bumps observed in the $z$-component of the velocity, depicted in Fig. 7, becomes visible. This boundary region is unstable, also under stationary solar wind conditions. The anisotropy in the velocity magnitude is caused by the nonzero $x$-component of the magnetic field. As sketched in Fig. 10, the plasma enters the wake either parallel or anti-parallel to the magnetic field lines because of the Frozen-in condition. In the sketch, the particles above the Moon are accelerated, particles below are decelerated. This is also in accordance to the observations during the WIND flyby (Ogilvie et al., 1996). Both plasma streams meet within the lunar wake, creating the unstable transition region.

The magnetic field, shown in panels (c), (f) and (i) of Fig. 9, shows a profile similar to the rarefaction wave in the density plots. While the magnitude of the magnetic field increases inside the wake, it is decreased in areas where the rarefaction wave expands. The amplitude of both, the inner increase and the outer decrease, becomes lower with increasing distance from the Moon.

### 4.4. MHD wave propagation

If the upstream conditions in the solar wind are constant, the downstream wake structure will remain stationary. The Moon just absorbs solar wind particles preventing them from propagating downstream, whereas the magnetic field diffuses through the Moon due to its low conductivity. Since thermal refilling processes cause only a small net flux of particles into the wake, the depletion is maintained over many lunar radii downstream.

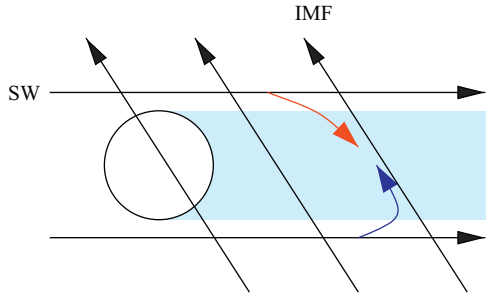


**Fig. 10.** Sketch of the asymmetry in the velocity magnitude. Particles enter the lunar wake parallel to the magnetic field. Particles above the Moon are accelerated (red), particles below the Moon are decelerated (blue). The effect is, thus, caused by the nonzero magnetic field component parallel to the solar wind. (For interpretation of the references to color in this figure legend, the reader is referred to the web version of this article.)

The sudden void of particles downstream of the Moon is probably the source of magnetohydrodynamic waves propagating across the wake. The three modes of MHD waves (fast, Alfvén and slow) cause different perturbations of the magnetic field and density. In the fast mode, which may expand in any direction, the magnetic field is compressed and correlated to the density. For the slow mode, magnetic field and density are anticorrelated and its expansion is mainly field-parallel. The Alfvén mode does not cause magnetic field compression and also expands mainly field-parallel.

The $yz$-plane of the simulation box is a transverse cut through the lunar wake where the expected waves are to be seen. The magnetic field vectors at this simulation plane are transformed into a field-aligned coordinate system, this allows for an easy separation of field-parallel and field-perpendicular components. Furthermore, the mean magnetic field strength is subtracted, so only the deviations from the mean field remain. Fig. 11 shows these deviations in a plane $4.8R_M$ downstream of the center of the Moon. The field-parallel component, shown in the left panel of Fig. 11, can have positive or negative signs. In case of the field-perpendicular component, shown in the right panel of Fig. 11, the variations are given as absolute values as 2D directional information cannot be included in this plot. Both components are expected to be zero in the undisturbed solar wind. The center of the fluctuations is not coincident with the origin the $yz$-plane as the solar wind velocity is not parallel to the Sun–Moon axis as seen in Fig. 8.

The superposed (white/black) boundaries in Fig. 11 represent the farthest possible propagation of fast, Alfvén and slow modes departing from the Moon's surface in the solar wind frame of reference. The outer circle encloses the phase fronts of a fast mode. The propagation velocity is computed based on the dispersion relations for MHD waves in warm plasma environments. The magnetosonic speed is given by $c_{ms}=\sqrt{v_a^2+c_s^2}$, where $v_a=59$ km/s is the Alfvén speed in the unperturbed solar wind and $c_s=v_a\cdot\sqrt{\gamma\beta/2}=34.9$ km/s is the sonic speed. For the adiabatic coefficient a value of $\gamma=2$ is assumed, in accordance to the simulation (Bößwetter et al., 2004, cf.). The plasma $\beta$ has been set to $\beta=(\beta_i+\beta_e)/2=0.35$. Since the depicted cross section has a distance ($x$-direction) from the Moon of $4.8R_M$, and the solar wind speed is of 297 km/s, the MHD modes have had a time of $t=28$ s to evolve in the solar wind. Therefore, the outer circle is apart from the innermost one by $c_{ms}\cdot t$ (in field-perpendicular direction), where the innermost circle represents the geometric wake: a circle of radius $R_M$ positioned according to the solar wind velocity vector.

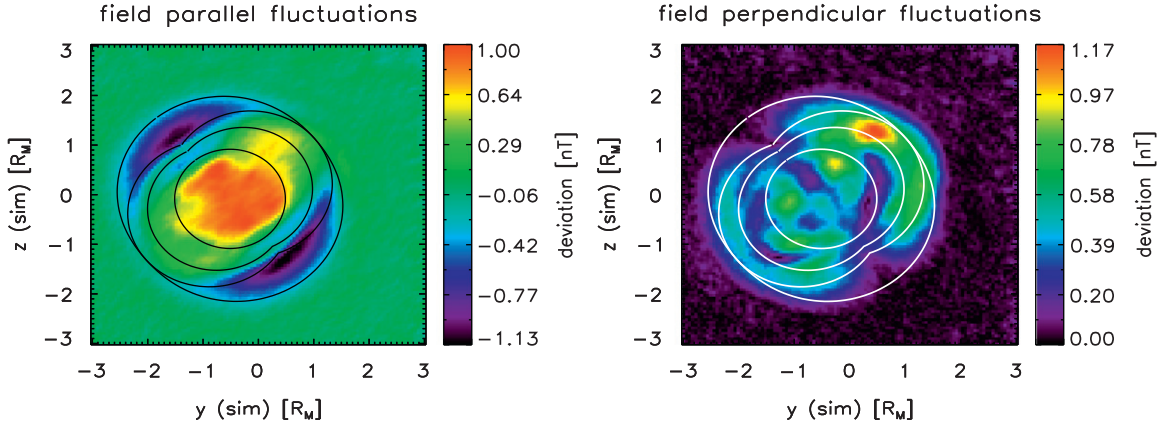


**Fig. 11.** Variations of the magnetic field in the $yz$-plane parallel (left panel) and perpendicular (right panel) to the background magnetic field direction. The drawings are the result of wave propagation computations for the MHD modes starting from the lunar surface and expanding to the given plane at $4.8R_M$.

The boundaries appear to be a Friedrichs (I) daigram; strictly spoken, this is not the case: While a Friedrichs diagram shows velocities of modes originating from a point source, the boundaries of Fig. 11 are the result of applying Huygens' principle to point sources at the lunar surface. For each angle around the inner circle, the plot shows the farthest propagation for each mode considering all point sources at a given time. This also explains why the boundaries of slow and Alfvén mode expand in field-perpendicular direction, this does not occur for a single point source depicted in a Friedrichs diagram.

The two boundaries between the circles enclose the Alfvén (intermediate) and slow mode maximum propagation areas. The Friedrichs diagram is well reproduced by the deviations of magnetic field and density in the cross sections shown, although the $x$-component of the magnetic field was not considered for the propagation estimations. As can be seen, the magnetic field depression is pronounced in the areas which are only enclosed by the outer circle (fast mode). This coincides with a region of lower particle density than in the solar wind and only very weak variations in field-perpendicular direction indicating a compressible disturbance. Due to the coincidence in less particles (less thermal pressure) and less magnetic pressure (negative variation) the disturbance in this area can be clearly identified with a fast mode; which is the only MHD mode that can penetrate into the indicated area in the given time of $t=28$ s (rarefaction fast mode wave). In field-aligned direction, depicted in the left panel of Fig. 11, between the slow mode boundary and the inner wake circle both field-parallel and field perpendicular variations in the magnetic field are present. The field-parallel variations are positive in sign indicating an increase in the magnetic field strength. Taking into account that the density is particularly depressed in this region the disturbance can be identified with a slow mode, for which magnetic and thermal pressure variations are anticorrelated. Between the slow mode and Alfvén mode boundaries, the magnetic field fluctuations are mainly field-perpendicular, as shown in the right panel of Fig. 11. The density is approaching the solar wind values: Therefore the disturbances are not compressible, but of Alfvénic nature. Note that this situation is different from Enceladus (Kriegel et al., 2009) or Io (Linker et al., 1988), where a standing Alfvén wave ("Alfvén wing") is triggered due to high conductivity regions.

With these magnetic field component plots, all three MHD modes were found in the lunar wake in the stationary simulation. Furthermore, the computed boundaries of farthest possible propagation are in good agreement to the simulation results.

## 5. Conclusions

In this work we have compared the results of a 3D hybrid plasma simulation to the data of the ARTEMIS P1 flyby and determined features of the lunar wake. For the first time, a real-time plasma simulation of the wake using dynamic solar wind data as input parameters has been successfully performed. For this simulation, the OMNI data were shifted in time to represent the SW $1.2R_M$ upstream by comparison with the ARTEMIS P1 data: A high degree of direct comparability was achieved.

The simulation is able to follow the solar wind variations and obtain good agreement with the data despite the highly variable solar wind upstream conditions. This was of special importance for the intercomparison with the magnetic field data, as the disturbance of the magnetic field by the Moon is in the order of only 10% of its strength and, thus, hardly to be seen within the strong IMF fluctuations. The additional stationary simulation combined with a comparison to the OMNI data allows a separation between the effects caused by solar wind fluctuations and effects caused by the presence of the Moon.

The comparison between data and simulation yielded several noticeable results. The general magnetic field structure for the lunar wake (Colburn et al., 1967; Whang and Ness, 1970) could be reproduced in stationary and dynamic situation. For the velocity, the counterstreaming structure in the wake (Ogilvie et al., 1996) as well as the perturbations in the wake center caused by this effect were found in data and simulations. For simulating this effect, a kinetic approach with the possibility of anisotropic velocity distributions was essential.

Also the results of the simulation of the lunar wake up to $4.8R_M$ behind the Moon were surveyed. Although the main plasma inflow direction is parallel to the magnetic field, we found that directly behind the Moon a rather symmetric refilling takes place. The magnetic field tilt causes an asymmetry in the velocity magnitude: Due to the nonzero $x$-component in the magnetic field, particles entering the lunar wake are either accelerated or decelerated, depending on their origin, also observed during the WIND flyby (Ogilvie et al., 1996).

By a wave propagation calculation, we showed that the structures in magnetic field and density coincide with the MHD modes. Fast, Alfvén and slow modes are present in the simulated wake, propagating at different speeds and directions depending on their well-known dispersion relations. Hence, the lunar wake can be regarded as a "théâtre vivant" representing a Friedrichs diagram for the three MHD modes. A flight with a S/C through the wake is a flight through a Friedrichs diagram in real space. As can be seen from the comparative plots of simulation and data, this fact is not obvious from the observations alone. A detailed simulation of the situation is needed to see how the data fit to the wake environment. The ARTEMIS mission may prove statistically by multiple wake crossings with two spacecrafts if this picture obtained from simulation is in fact present as expected.

## Acknowledgements

This work has been supported by the Deutsche Forschungsgemeinschaft (DFG) through grant MO539/17-1. The work of U.M. and J.M. was supported by the DFG under grant number MO539/16-1. The simulations were performed on the systems of the North-German Supercomputing Alliance. Financial support for the work of the FGM Lead Investigator Team at the Technical University of Braunschweig by the German Ministerium für Wirtschaft und Technologie and the Deutsches Zentrum für Luft- und Raumfahrt under grant 50OC1001 is acknowledged. ARTEMIS was made possible by NASA under contract NAS5-02099.

## References

Angelopoulos, V. The ARTEMIS Mission. Space Sci. Rev., in press. doi:10.1007/s11214-010-9687-2.

Auster, H.U., Glassmeier, K.H., Magnes, W., Aydogar, O., Baumjohann, W., Constantinescu, D., Fischer, D., Fornacon, K.H., Georgescu, E., Harvey, P., Hillenmaier, O., Kroth, R., Ludlam, M., Narita, Y., Nakamura, R., Okrafka, K., Plaschke, F., Richter, I., Schwarzl, H., Stoll, B., Valavanoglou, A., Wiedemann, M., 2008. The THEMIS fluxgate magnetometer. Space Sci. Rev. 141, 235–264.

Bagdonat, T., Motschmann, U., 2002. 3D hybrid simulation code using curvilinear coordinates. J. Comput. Phys. 183, 470–485.

Birch, P.C., Chapman, S.C., 2002. Two dimensional particle-in-cell simulations of the lunar wake. Phys. Plasmas 9, 1785–1789.

Bößwetter, A., Bagdonat, T., Motschmann, U., Sauer, K., 2004. Plasma boundaries at Mars: a 3-D simulation study. Ann. Geophys. 22, 4363–4379.

Colburn, D.S., Currie, R.G., Mihalov, J.D., Sonett, C.P., 1967. Diamagnetic solar-wind cavity discovered behind Moon. Science 158, 1040–1042.

Dyal, P., Parkin, C.W., Daily, W.D., 1974. Magnetism and the interior of the Moon. Rev. Geophys. Space Phys. 12, 568–591.

Farrell, W.M., Kaiser, M.L., Steinberg, J.T., Bale, S.D., 1998. A simple simulation of a plasma void: applications to Wind observations of the lunar wake. J. Geophys. Res. 103, 23653–23660.

Georgescu, E., Plaschke, F., Auster, H., Frey, H. Modelling of spacecraft spin period during eclipse. Ann. Geophys., in review.

Halekas, J.S., Lin, R.P., Mitchell, D.L., 2005. Large negative lunar surface potentials in sunlight and shadow. Geophys. Res. Lett. 32, L09102.
Halekas, J.S., Mitchell, D.L., Lin, R.P., Hood, L.L., Acuña, M.H., Binder, A.B., 2002. Evidence for negative charging of the lunar surface in shadow. Geophys. Res. Lett. 29, 1435.
Hartle, R.E., Killen, R., 2006. Measuring pickup ions to characterize the surfaces and exospheres of planetary bodies: applications to the Moon. Geophys. Res. Lett. 33, L05201.
Huixian, S., Shuwu, D., Jianfeng, Y., Ji, W., Jingshan, J., 2005. Scientific objectives and payloads of Chang'E-1 lunar satellite. J. Earth Syst. Sci. 114, 789–794.
Kallio, E., 2005. Formation of the lunar wake in quasi-neutral hybrid model. Geophys. Res. Lett. 32, L06107.
Kato, M., Sasaki, S., Takizawa, Y., 2010. The Kaguya mission overview. Space Sci. Rev., 1–17.
Kriegel, H., Simon, S., Müller, J., Motschmann, U., Saur, J., Glassmeier, K.-H., Dougherty, M.K., 2009. The plasma interaction of Enceladus: 3D hybrid simulations and comparison with Cassini MAG data. Planet. Space Sci. 57, 2113–2122.
Linker, J.A., Kivelson, M.G., Walker, R.J., 1988. An MHD simulation of plasma flow past Io—Alfven and slow mode perturbations. Geophys. Res. Lett. 15, 1311–1314.
Lipatov, A.S., Motschmann, U., Bagdonat, T., Grießmeier, J., 2005. The interaction of the stellar wind with an extrasolar planet—3D hybrid and drift-kinetic simulations. Planet. Space Sci. 53, 423–432.
Lyon, E.F., Bridge, H.S., Binsack, J.H., 1967. Explorer 35 plasma measurements in the vicinity of the Moon. J. Geophys. Res. 72, 6113–6117.
McFadden, J.P., Carlson, C.W., Larson, D., Ludlam, M., Abiad, R., Elliott, B., Turin, P., Marckwordt, M., Angelopoulos, V., 2008. The THEMIS ESA plasma instrument and in-flight calibration. Space Sci. Rev. 141, 277–302.
Nath Goswami, J., Annadurai, M., 2008. Chandrayaan-1 mission to the Moon. Acta Astronaut. 63, 1215–1220.
Ness, N.F., 1965. The magnetohydrodynamic wake of the Moon. J. Geophys. Res. 70, 517–534.
Ness, N.F., Behannon, K.W., Scearce, C.S., Cantarano, S.C., 1967. Early results from the magnetic field experiment on Lunar Explorer 35. J. Geophys. Res. 72, 5769–5778.
Ness, N.F., Scearce, C.S., Seek, J.B., 1964. Initial results of the Imp 1 magnetic field experiment. J. Geophys. Res. 69, 3531–3569.
Ogilvie, K.W., Steinberg, J.T., Fitzenreiter, R.J., Owen, C.J., Lazarus, A.J., Farrell, W.M., Torbert, R.B., 1996. Observations of the lunar plasma wake from the WIND spacecraft on December 27, 1994. Geophys. Res. Lett. 23, 1255–1258.
Richmond, N.C., Hood, L.L., 2008. A preliminary global map of the vector lunar crustal magnetic field based on Lunar Prospector magnetometer data. J. Geophys. Res. 113, E02010.
Roussos, E., Müller, J., Simon, S., Bößwetter, A., Motschmann, U., Krupp, N., Fränz, M., Woch, J., Khurana, K.K., Dougherty, M.K., 2008. Plasma and fields in the wake of Rhea: 3-D hybrid simulation and comparison with Cassini data. Ann. Geophys. 26, 619–637.
Saito, Y., Yokota, S., Asamura, K., Tanaka, T., Nishino, M.N., Yamamoto, T., Terakawa, Y., Fujimoto, M., Hasegawa, H., Hayakawa, H., Hirahara, M., Hoshino, M., Machida, S., Mukai, T., Nagai, T., Nagatsuma, T., Nakagawa, T., Nakamura, M., Oyama, K., Sagawa, E., Sasaki, S., Seki, K., Shinohara, I., Terasawa, T., Tsunakawa, H., Shibuya, H., Matsushima, M., Shimizu, H., Takahashi, F., 2010. In-flight performance and initial results of plasma energy angle and composition experiment (PACE) on SELENE (Kaguya). Space Sci. Rev., 1–39.
Samir, U., Wright Jr., K.H., Stone, N.H., 1983. The expansion of a plasma into a vacuum: basic phenomena and processes and applications to space plasma physics. Rev. Geophys. Space Phys. 21, 1631–1646.
Sibeck, D.G., Angelopoulos, V., 2008. THEMIS science objectives and mission phases. Space Sci. Rev. 141, 35–59.
Sibeck, D.G., Angelopoulos, V., Delory, G., Eastwood, J., Farrell, W., Grimm, R., Halekas, J., Hasegawa, H., Hellinger, P., Khurana, K., Lillis, R., Øieroset, M., Phan, T., Raeder, J., Russell, C., Schriver, D., Slavin, J., Travnicek, P., Weygand, J. ARTEMIS science objectives and mission phases. Space Sci. Rev., in review.
Simon, S., Saur, J., Neubauer, F.M., Motschmann, U., Dougherty, M.K., 2009. Plasma wake of Tethys: hybrid simulations versus Cassini MAG data. Geophys. Res. Lett. 36, L04108.
Trávníček, P., Hellinger, P., Schriver, D., Bale, S.D., 2005. Structure of the lunar wake: two-dimensional global hybrid simulations. Geophys. Res. Lett. 32, L06102.
Whang, Y.C., Ness, N.F., 1970. Observations and interpretation of the lunar Mach cone. J. Geophys. Res. 75, 6002–6010.